Topology and Sizing Optimization of Thermal and Electric Energy Systems for Battery Electric Vehicle

Fakher Belkacem, Henrik Schäfer, Tobias Hellberg, Martin Meywerk
Helmut Schmidt University Hamburg / Professorship for Automotive Engineering
Holstenhofweg 85, 22043 Hamburg
fakher.belkacem@hsu-hh.de Henrik.schaefer@hsu-hh.de tobias.hellberg@hsu-hh.de
Martin.meywerk@hsu-hh.de

Abstract: The transition to battery electric vehicles requires electrification of power systems. The reliability and efficiency of electrical conversion systems are often compromised due to inadequate thermal management systems, leading to electronic failures and performance degradation. Addressing this challenge necessitates the optimization of thermal systems and the development of innovative vehicle architectures. The proposed study utilizes a novel design framework for topology and sizing optimization of electric vehicle energy systems using a graph-based modeling approach. To address the increasing complexity of electric vehicle systems, the model incorporates multi-physics modeling, integrating the interaction between the thermal, electrical, and mechanical domains. Additionally, the framework uses energy conservation laws to capture physical system dynamics, making optimization more structured and helping analyze design trade-offs effectively. To demonstrate its effectiveness, an electric bus powertrain design is investigated as a case study, with the goal of optimizing thermal and electrical component sizes and energy flow, as well as discrete choices in the topology of the system. The electric bus model incorporates experimentally validated empirical data obtained through advanced measurement techniques, ensuring credible optimization and realistic system behavior. This case study demonstrates how design optimization can influence the efficiency of thermal management systems.

1 Introduction

The rapid growth of electric mobility is creating new challenges for vehicle design. Engineers now face increasingly complex systems in which electrical, thermal, and mechanical domains strongly interact. To address this complexity, advanced frameworks are required that support system-level optimization. Several approaches have been developed for modeling the dynamics of such physical systems, including state-space models [1], partial differential equations [2, 3], bond graphs [4], and block diagram modeling techniques [5].

Contribution: 2025 FKFS Conference on Vehicle Aerodynamics and Thermal Management
15 – 16 October 2025 | Leinfelden-Echterdingen

These methods differ in their modularity, computational complexity, and ability to capture interactions between subsystems. A major difficulty in applying physics-based models to optimization lies in integration: because models from different disciplines often exchange information through incompatible signals, communication and simultaneous simulation across domains can become challenging [6].

To overcome these limitations, this paper applies a conservation-based optimization framework for dynamic systems of systems. The proposed approach builds on the graph-based modelling methodology developed by [7], which can be adapted to the generic formulation introduced by [8]. This procedure is further augmented by [9] to enable design optimization frameworks for systems governed by conservation laws. The modeling techniques are physics-based, modular, and designed to capture interactions across multiple domains [10].

The applicability of the graph-based methodology has already been demonstrated in several studies. For example, [8] shows its effectiveness in modeling a hybrid electric UAV powertrain and designing predictive control strategies, while other works validate its ability to capture the dynamics of thermal–fluid systems against experimental data [7]. Building on this foundation, another work of [9] applies the augmented graph-based framework to the optimization of battery-electric vehicles, investigating the influence of different configurations and component dimensions on energy efficiency and system mass. A hybrid electro-thermal energy storage system is also introduced as a representative design example, highlighting the benefits of employing the framework for system-level optimization of both plant and controller [11].

While system-level optimization of battery-electric vehicles has received attention in the literature, notably absent are results derived from real world data validating the capabilities of this framework as well as the realization of the impact of optimization frameworks on thermal management systems.To address this gap, the framework is instantiated here on a Battery Electric Vehicle (BEV) bus powertrain under realistic operating conditions. Here, electrical and thermal components are jointly optimized.

This leads to the following key contributions of the paper: → Formulation of a general graph-based framework for multi-domain, multi-objective optimization, enabling consistent representation and integration of several subsystems based on fundamental works of Alleyne e.g. [7-14] → Demonstration on a realistic BEV bus architecture, including strong electrical–thermal couplings, to illustrate the framework's workflow and applicability to real-world design problems→ Numerical case studies showcasing the potential of the proposed approach to improve thermal management systems, highlighting its capacity to handle coupled domains and system-level objectives.

2 Graph-Based Modeling Basics

This section introduces graph-based modeling [12, 13, 14] and outlines design optimization for these models [9].

2.1 Graph-Based Modeling

The graph-based models are derived by applying conservation equations to a component or system, inherently capturing the storage and transport of energy [15]. In such a representation, energy storing capacitive elements are modeled as vertices, while the paths for energy transport between storage elements (the vertices) are modeled as edges. An important feature that enhances the suitability of graph-based models is their capacity to incorporate orientation, which permits bidirectional power exchange between vertices. For example, in battery electric vehicle energy transfer occurs in both directions from the battery to drive the vehicle and back to the battery during braking (brake energy recuperation), which can be modelled by bidirectional graphs. The orientation of an edge defines only the reference direction for positive power flow. Each edge e_j is associated with a bidirectional power transfer p_j, which may depend nonlinearly on the states of the adjacent vertices and, if applicable, on an actuator input.

$$p_j = f_j\left(x_j^{\text{tail}}, x_j^{\text{head}}, u_j\right). \tag{1}$$

Here, $\mathrm{x}_j^{\text{tail}}$and x_j^{head} denote the states of the tail and head vertices of edge j. Applying conservation of energy to a state x_i at vertex v_i gives the following dynamic equation:

$$C_i \dot{x}_\iota = p_i^{\text{in}} - p_i^{\text{out}}, \tag{2}$$

where $C_i \geq 0$ is the vertex capacitance, and p_i^{in} and p_i^{out} are the total incoming and outgoing power flows at vertex i. Appling the previous equation for all states, the full system dynamics can be rewritten as

$$\boldsymbol{C}\dot{\boldsymbol{x}} = -\overline{\boldsymbol{M}}\boldsymbol{p} + \overline{\boldsymbol{D}}\boldsymbol{p}^{\text{s}}, \tag{3}$$

where $\boldsymbol{x}$ ist the state vector, $\overline{\boldsymbol{M}}$ maps the edges to the vertices, $\overline{\boldsymbol{D}}$ describes the relationship between the sources and the vertices and $\boldsymbol{p}^s$ is a vector of external power flow and $\boldsymbol{C}$ is a matrix of vertex capacitances [7]. The states and the capacitances used for the case study are discussed in detail in Section 3.

However the graph based model described by Eq.(3) is not suitable for design optimization as it is. The next section is limited to the latter.

2.2 Design Optimization

To perform an optimization framework, the system must be expressed in terms of design variables, which serve as the fundamental degrees of freedom guiding the search for improved performance. Within a graph-based modeling approach, the influence of design variables manifests in two principal forms: modifications of component size and modifications of system topology. From a graph-theoretic perspective, the size of a component is encoded in the capacitance matrix, which governs the system’s dynamic behaviour. Scaling the size of a vertex not only affects the vertex itself but also the connected edges, the resulting power flow, and ultimately the source contributions.

For example, increasing the battery capacity Q modifies its internal resistance R, which in turn changes the dissipated heat according to RI^2. This illustrates the principle of sizing optimization, where adjustments in design variables propagate through both local interactions and the global system response. In contrast, topology optimization focuses on exploring alternative system configurations through the addition or removal of edges. Such modifications affect the same three aspects as in sizing optimization—vertex properties, edge weights, and source-edge contributions—and therefore must be analyzed with equal care to preserve system consistency and physical feasibility.

The formal relationship between design variables and system dynamics is captured in the augmented graph-based model [9]. Its matrix form is expressed in Eq.(4):

$$\boldsymbol{\Psi}_c \boldsymbol{\Phi}_c \boldsymbol{C} \dot{\boldsymbol{x}} = -\bar{\boldsymbol{M}} \boldsymbol{\Psi} \boldsymbol{\Phi} \boldsymbol{p} + \boldsymbol{D} \boldsymbol{\Psi}^s \boldsymbol{\Phi}^s \boldsymbol{p}^s. \tag{4}$$

The six design matrices $\boldsymbol{\Psi}_c$, $\boldsymbol{\Phi}_c$, $\boldsymbol{\Psi}$, $\boldsymbol{\Phi}$, $\boldsymbol{\Psi}^s$and $\boldsymbol{\Phi}^s$ map the effects of component scaling and alternative architectures into the mathematical representation of the model. Specifically, $\boldsymbol{\Psi}_c$ and $\boldsymbol{\Phi}_c$ capture the influence of sizing and topology decisions on vertex properties. The matrices $\boldsymbol{\Psi}$ and $\boldsymbol{\Phi}$ represent the corresponding effects on edge scaling and removal, while $\boldsymbol{\Psi}^s$ and $\boldsymbol{\Phi}^s$ account for these effects on the source edges of the graph-based model. These design matrices are diagonal and contain design functions that depend on the design variables. For further details cf. [9].

2.4 Formulating the Optimization Problem

The core of this framework lies in formulating and solving the optimization problem, which can be expressed as follow

$$\begin{aligned} &\min_{\boldsymbol{\theta}} \; \mathrm{J}_{\mathrm{total}}(\boldsymbol{\theta}_{\mathbf{c}}, \boldsymbol{\theta}_{\mathbf{z}}) \\ &\text{subj. to}: \quad \underline{\boldsymbol{\theta}} \leq \boldsymbol{\theta} \leq \overline{\boldsymbol{\theta}}, \\ &g(\boldsymbol{\theta}) \leq \mathbf{0} \end{aligned} \tag{5}$$

Here, $\mathrm{J}_{\mathrm{total}}(\boldsymbol{\theta}_{\mathbf{c}}, \boldsymbol{\theta}_{\mathbf{z}})$ denotes the objective function, which may serve various optimization purposes, such as minimizing mass, reducing energy losses, or enhancing overall performance. The design vector $\boldsymbol{\theta}$ comprises the sizing and topology-related design variables, $\boldsymbol{\theta}_{\mathbf{c}}$ and $\boldsymbol{\theta}_{\mathbf{z}}$, respectively and is defined as

$$\boldsymbol{\theta} = \begin{pmatrix} \boldsymbol{\theta}_{\mathbf{c}} \\ \boldsymbol{\theta}_{\mathbf{z}} \end{pmatrix}. \tag{6}$$

This vector is defined within specified bounds, such that each variable must remain between a given lower limit $\underline{\boldsymbol{\theta}}$ and upper limit $\overline{\boldsymbol{\theta}}$. The previously discussed augmented modelling approach is employed within the optimization problem, where the graph-based model is simulated for a given set of design variables and the objective function is evaluated from the resulting trajectories.

Eq. (5) presents also the set of nonlinear constraints with nonlinear function g for the design problem.

In the following section, this proposed optimization procedure is demonstrated through its application to a real-world battery electric bus.

3 Design of an Electric Vehicle Powertrain

This section applies the design optimization framework to a case study of a bus powertrain configuration, considering electrical, mechanical, and thermal power flows, with data experimentally validated in [16]. The baseline configuration, including sizing and architecture options, is outlined and represented as a graph based model. These configuration options are then formulated as an optimization problem within the framework, where different single- and multi-objective functions are defined. The results highlight the capability of the framework to identify designs that meet different requirements.

3.1 Configuration of the Bus Electric Powertrain

Fig 1 presents the baseline EV powertrain configuration, and Figs. 2–4 show the graphical models of the three parts of the powertrain.

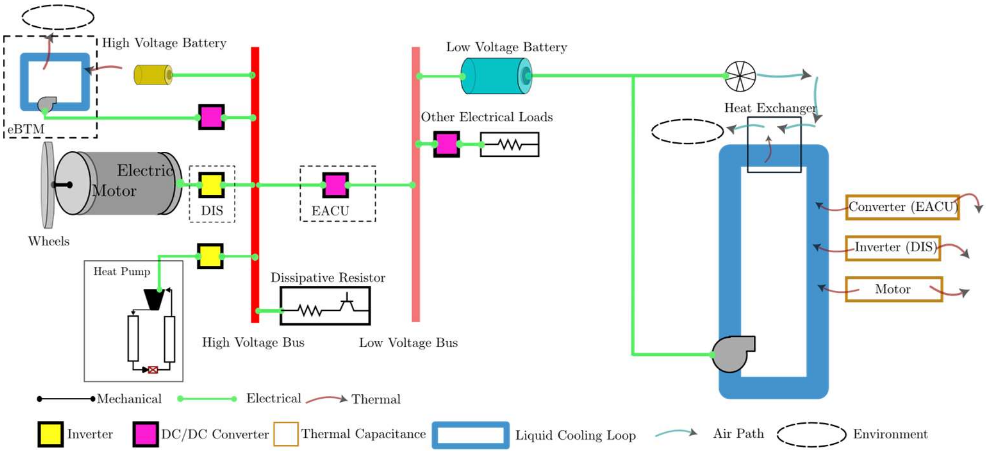

Figure 1: Electric vehicle baseline powertrain configuration.

The powertrain consists of a battery system as the main power source, connected in parallel to a high-voltage direct current (DC) bus. This bus distributes power to three subsystems: (i) the Drive Inverter System (DIS), which drives an AC motor responsible for vehicle propulsion; (ii) an inverter that supplies the HVAC system (heating, ventilation, and air conditioning); (iii) an Electronic Accessory Control Unit (EACU) and (iiii) an electric battery thermal management module (eBTM) to fulfil the conditional needs of the battery. Note that eBTM is not modeled in this case study.

In addition, the high-voltage bus is connected through a switch to a dissipative resistor that prevents overvoltage events.

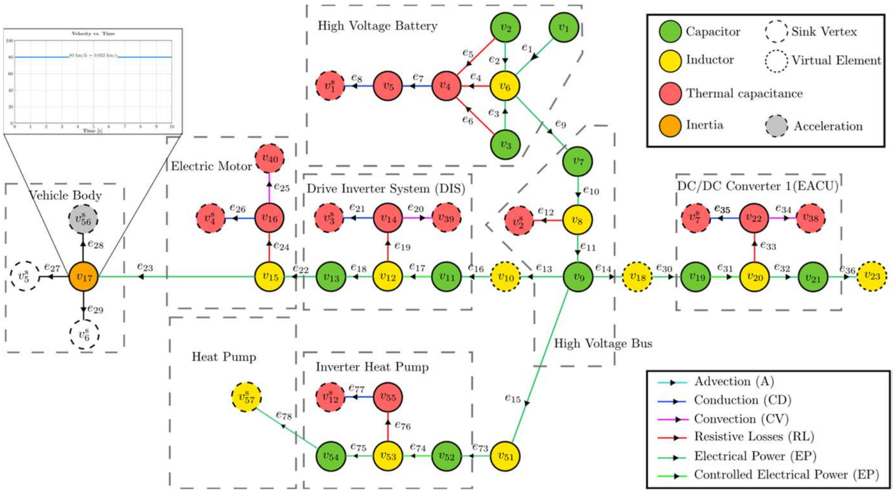

Figure 2: Graph-based model of high voltage bus (battery, motor and vehicle body).

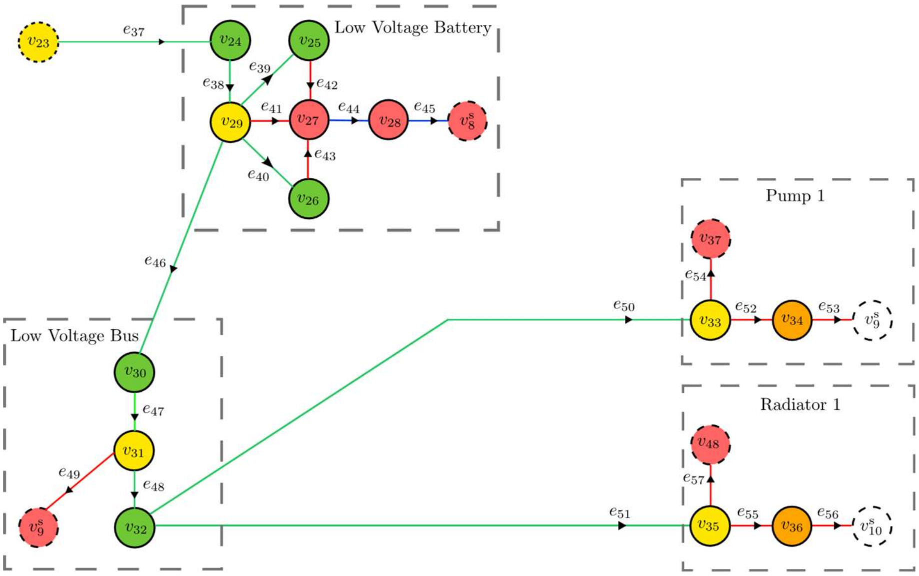

Figure 3: Graph-based model of the low voltage bus

The EACU, implemented as a bidirectional DC/DC converter, steps the voltage down to supply a low-voltage DC bus. This low-voltage bus both charges a 24 V auxiliary battery and powers additional electrical loads. The auxiliary battery in turn drives the cooling pump, which circulates coolant through the liquid cooling loop of the drive system, and the fan, which extracts heat from the coolant via a heat exchanger to the ambient environment.

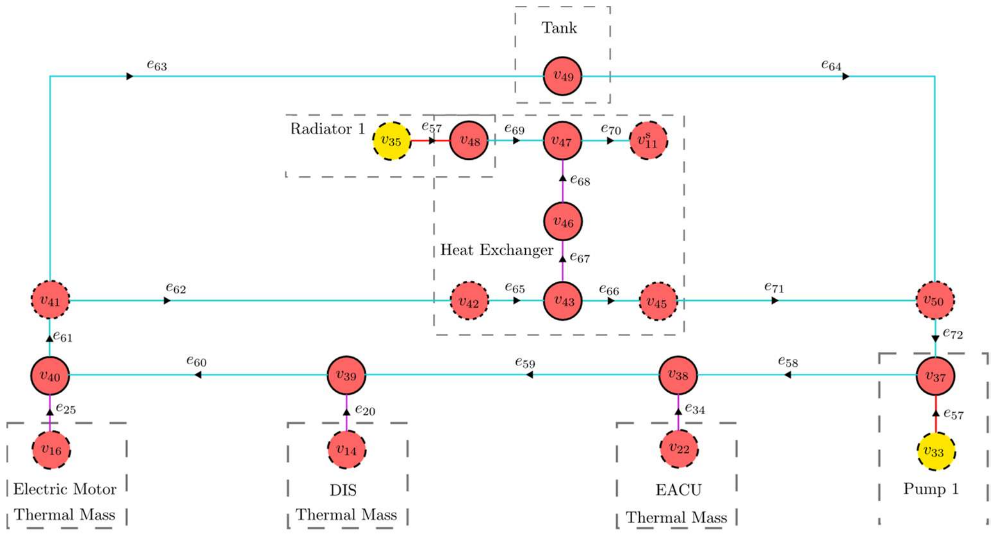

Figure 4: Graph-based of the Cooling System

Inputs to the system include the duty cycles of the three inverters/converters. The duty cycles of the DIS and the HVAC inverter are held constant to satisfy the required vehicle speed and the HVAC load demand, respectively. By contrast, the duty cycle of the EACU is controlled to ensure the auxiliary battery is charged with exactly the power required by the pump and the radiator.

In this study, the pump and radiator rotational speeds, as well as the vehicle velocity, are kept constant. This assumption allows the investigation of a single operating point. Switch input commands include (i) the buck/boost directionality for each of the three converters and (ii) the connection command for the dissipative resistor. For the considered case study, all converters are fixed in buck mode. Disturbances (sink states) include ambient air temperature, the current demand by the HVAC system, and the vehicle's velocity demand profile.

For clarity, the definitions of the state vector p and the connection matrix C (in Eq. (4)) varies depending on its type as specified in Table 1.

Table 1: Vertex types and capacitances.

Description	State	Capacitance
Voltage	V	$C_{\mathrm{v}}V$
Battery state of charge	q	$QV_{\mathrm{ocv}}(q)$
Current	I	LI
Temperature	T	C_{T}
Translating Mass	v	mv

The elements capacitance's are electrical capacitance C_T, inductance L, mass m, battery capacitance QV_ocv and thermal capacitance C_v. Note that, Q represents the battery capacity and V_ocv is the open circuit voltage of the battery. This graph contains vertices corresponding to battery state of charge (SOC), current, voltage, temperature and velocity. In Figures (2), (3) and (4), the voltage, temperature, and velocity states are indicated by green, yellow, and orange vertices, respectively.

The state battery state of charge (SOC) are given by the vertices v_1 and v_{24} in the Figures. (2) and (3), respectively. There are six types of edges in this graph representing different mechanisms of power transfer: electrical power, controlled electrical power, resistive losses, advection, conduction, and convection. Power flows of the same type follow similar governing equations, as specified by the corresponding edges in Table 2.

This case study explores three sizing design options. The next section relates these design options to the graph-based model within the proposed framework.

Table 2: Power flow edge equations by type.

Edge Type	Edge equation	Corresponding edge numbers
Electrical power	$P_j = x_j^\text{tail} x_j^\text{head}$	1-3, 9-11, 13-16, 18, 22, 23, 30, 32, 36, 73, 75, 78, 37-40, 46, 48, 50, 51
Controlled electrical power	$P_j = u_j x_j^\text{tail} x_j^\text{head}$	17, 31, 47
Resistive losses	$P_j = k_j \left(x_j^\text{tail}\right)^2$	4, 5, 6, 12, 19, 24, 33, 42, 41, 43, 49, 52, 54, 55,
Advection	$P_j = k_j u_j x_j^\text{tail}$	58–66, 69, 70
Conduction	$P_j = k_j \left(T_j^\text{tail} - T_j^\text{head}\right)$	7, 8, 21, 26, 35, 77
Convection	$P_j = k_j \left(x_j^\text{tail} - x_j^\text{head}\right)$	20, 25, 34, 67, 68

a For edge 1 and 24, $x_j^\text{tail} = V_\text{ocv}\left(x_j^\text{tail}\right)$, where V_ocv is the corresponding battery open circuit voltage.

b. For edge 37: $x_j^\text{head} = V_\text{ocv,l}\left(x_j^\text{head}\right)$, where $\text{V}_\text{ocv,l}$ is the open circuit voltage of the low voltage battery.

b Example of controlled electrical power for edge 17: U *and* I represent voltage and current at two ends of the edge and u represents the duty cycle oft the Driving Inverter System (DIS).

3.2 Applying the Framework to the Battery Electric Vehicle Bus Powertrain

The discussed design optimization framework is applied to the case study system and requires at first step the definition of the design variables, which are described in Eq. (7). The used design function is

$$\mathfrak{f}\left(\theta_{\text{c},\sigma}, \mu\right) = 1 + 4\,\mu\,\theta_{\text{c},\sigma}, \tag{7}$$

and establishes a relationship between a design variable $\theta_{c,\sigma}$ and an output $\mathfrak{f}$. The first design option in this case study includes size of the battery ($\theta_{\mathrm{c},1}$). Sizing of the battery is considered analogous to adding fractions of cells in parallel n_{par}, which directly affects battery parameters such as capacity and mass. To reflect this, the first entry of $\boldsymbol{\Psi}_c$ in Eq.(4) is defined as:

$$f_{\psi_{c,1}}\left(\theta_{c,1}\right) = n_{\mathrm{par}}\left(\theta_{c,1}\right) = n_{\mathrm{par,nom}}\ \mathfrak{f}\left(\theta_{c,1}, \mu_{\mathrm{n_{par}}}\right). \tag{8}$$

Here, $\mu_{\mathrm{n_{par}}}$ is set to 0.47, ensuring that the number of parallel cells n_{par} varies between 6 and 18. The nominal number of parallel cells in the high-voltage battery, $n_{\mathrm{par,nom}}$, is defined as 6. Important information is that the size of the series cells is kept constant during the optimization procedure to ensure the required voltage level for the driving motor. As the number of parallel cells in a battery pack increases, both the electrical capacity (vertices: v_2, v_3) and the thermal mass (vertices: v_4, v_5) scale proportionally. The internal resistance of the battery is also influenced by the overall pack size, which is modeled in edge e_4. The design functions applied in this study are described in detail in [9].

The parameters $\theta_{\mathrm{c},2}$ and $\theta_{\mathrm{c},3}$ are introduced to model the scaling of the motor and pump sizes, respectively. An increase in these parameters corresponds to an increase in the motor constant, which in turn leads to higher resistance in the associated components. Note that the motor constant defines the torque a motor can supply per unit of current. Using the design function in Eq.(7) captures this effect, as illustrated in Fig. (5).

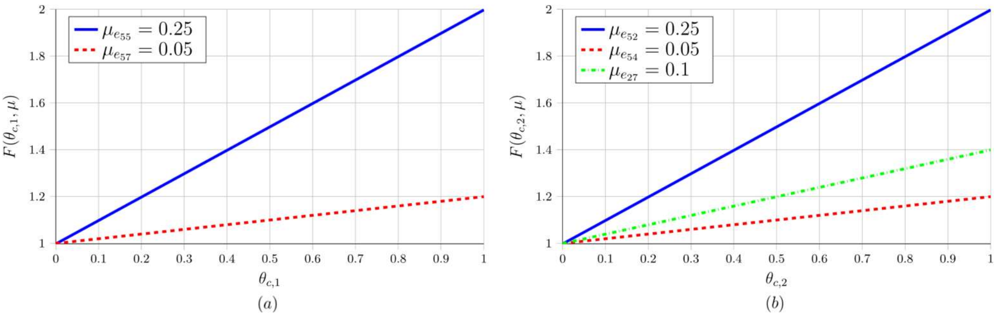

(a)

(b)

Figure 5: Design functions for component parameters. (a) Pump parameters and (b) motor parameters (blue: motor constant, red: resistance, green: mass).

Motor mass increases with scaling, thereby contributing to the total vehicle mass, which is used to compute the power flow from rolling and gradient resistances at edge e_{27}. The acceleration resistance is not considered in this study, as a constant driving velocity is assumed. As shown in Figure (5.a), the pump mass is considered negligible and has no impact on the model. The primary effects occur at edges e_{55} and e_{57}, where scaling the motor constant results in increased pump resistance.

In the next step of the framework is to define the total objective function, which is defined as

$$J_{\text{Total}} = w_1\, J_{\text{EL,p}} + w_2\, J_{\text{mass}} + w_3\, J_{\text{Driving}} + w_4\, J_{\text{EL,m}} + w_5\, J_{\text{perf}}, \tag{9}$$

Here, $J_{EL,p} = R_{\text{pump}}\, f_{\psi_{54}}(\theta_{c,1}) I_{\text{pump}}^2$, minimizes the energy losses through the pump where $R_{\text{pump}}\ and\ I_{\text{pump}}$ denotes the resistance of the pump and the current supplied to the pump, respectively. J_{mass} minimizes the mass of the vehicle and is defined as

$$J_{\text{mass}} = \frac{m_0 + m_{\text{motor}} \cdot f(\theta_{\text{c},2}, \mu_{e_{27}}) + \text{n}_{\text{ser}} \cdot m_{\text{cell}} \cdot n_{\text{par,nom}} \cdot f(\theta_{\text{c},1}, \mu_{n_{par}})}{m_{\text{ref}}}. \tag{10}$$

In this formulation, m_{ref} denotes the reference mass of the vehicle, taken as its initial mass. The parameters n_{ser} and $n_{\text{par,nom}}$ represent the number of battery cells connected in series and the nominal number of cells connected in parallel, respectively. m_{cell} corresponds to the mass of a single battery cell and m_{motor} is the mass of the driving motor. Eq.(9) considers also

$$J_{\text{Driving}} = \frac{\left(f(\theta_{\text{c},1}=1, \mu_{\text{n}_{\text{par}}}) - f(\theta_{\text{c},1}, \mu_{\text{n}_{\text{par}}})\right)^2}{f(\theta_{\text{c},1}=1, \mu_{\text{n}_{\text{par}}})}, \tag{11}$$

which is used as a penalty term to satisfy design constraint, ensuring that the vehicles reach a maximum driving range. $J_{\text{EL,m}}$ evaluates the efficiency and effectiveness of the electrical motor, where optimization leads to reduced losses and better reliability. This function is defined as $J_{\text{EL,m}} = \frac{(R_{\text{motor}}\, f(\theta_{c,2}, \mu_{e_{54}}) I_{\text{motor}}^2)}{R_{\text{motor}} I_{\text{motor}}^2}$.

In this equation, R_{motor} represents the electrical resistance of the motor, while I_{motor} denotes the electrical current supplied to the motor. Last but not least, J_{perf} in Eq.(12) aggregates overall performance measures not explicitly included in the other terms, ensuring balanced system performance.

$$J_{\text{perf}} = \frac{\left(P_{\text{motor,max}}(\theta_{\text{c},2} = 1) - P_{\text{motor,actue}}\ (\theta_{\text{c},2})\right)^2}{P_{\text{motor,max}}(\theta_{\text{c},2} = 1)}, \tag{12}$$

In this formulation, $P_{\text{motor,actuell}}$ denotes the actual motor power as a function of the operating parameter $\theta_{\text{c},2}$. The term $P_{\text{motor,max}}$ corresponds to the maximum motor power, which is reached when $\theta_{\text{c},2}$ approaches its limiting value. However, the design variables have been normalized. For $\boldsymbol{\theta} = [\theta_{\text{c},1}, \theta_{\text{c},2}, \theta_{\text{c},3}]$, the bounds are $\mathbf{0} \leq \boldsymbol{\theta} \leq \mathbf{1}.$ The framework can now be applied, with the full problem formulated in the same manner as Eq. (5). For the dynamic simulation, the vehicle is driven at a constant velocity of 80 km/h, with the state of charge (SOC) set to 80% for both the high-voltage and low-voltage batteries, and all component temperatures are initialized to the ambient value.

The system dynamics are integrated using MATLAB's ode15s solver. For the optimization, MATLAB's sequential quadratic programming (SQP) algorithm is used to determine the optimal system configuration.

3.4 Results

The design framework is evaluated using three different sets of objective function weights. Test 1 emphasizes minimizing energy losses through the pump ($J_{\mathrm{EL,p}}$), while Test 2 minmizes the mass of the vehicle (J_{mass}) and maximize the driving range (J_{Driving}), which is assumed to be used as design contain in the objective function. Test 3 uses the same objective of optimization of test 2 and places additionally focus in the minimizing of the electric motor ($J_{\mathrm{EL,m}}$) with consideration of the penalty term to the total objective in order to maximize the motor power (J_{perf}). Table 3 presents the weights for each tests. Table 4 presents the design parameter values and the number of iterations for the three tests.

Table 4: Weights for the three test.

Weight	Test 1	Test 2	Test 3
w_1	1	0	0
w_2	0	0.5	0.5
w_3	0	0.09	0.08
w_4	0	0	0.5
w_5	0	0	0.01

The evolution of the objective functions is illustrated in Fig. (6.a). In all cases, the objective function decreases during the optimization process, indicating that SQP converges to an improved design compared to the initial configuration. Test 1 converges after three iterations, whereas Test 3 and Test 4 require five and eight iterations, respectively, due to the higher complexity of the multi-objective optimization.

Test 1 results in an increased pump size, since the design variable $\theta_{\mathrm{c},3}$ reaches its upper bound. This outcome is in line with expectations, since enlarging the pump increases the motor constant, thereby reducing the current required to drive the pump for cooling the liquid. Although a larger pump also leads to higher resistance, the current appears squared in the expression of energy losses, so the overall effect remains beneficial. As a result the used thermal management system will need less power to cool the drive system. In Test 2, the optimizer slightly increases the number of parallel battery cells, reflecting the high weight on the driving-range term w_3. Lowering w_3 reduces the incentive to add parallel cells and thus decreases battery-pack/vehicle mass.

Table 3: Optimization Results

	Test 1		Test 2		Test 3	
	Initial values	Optimized values	Initial values	Optimized values	Initial values	Optimized values
$\theta_{c,1}$	0.0	-	0.5	0.7174	0.5	0.6821
$\theta_{c,2}$	0.0	–	0.5	0	0.5	0.9754
$\theta_{c,3}$	0.5	1	0.0	-	0.5	-
Normalized obj. func	1.58	0.20	1.87	0.009	2.42	1.11
Number of iterations	–	3	-	5	-	8

Test 3 confirms this behaviour: with the same objective structure but a smaller w_3, the optimizer selects a lower mass-scaling parameter, $\theta_{\mathrm{c},1} = 0.6821$, relative to Test 2, indicating a reduced vehicle mass. The results, illustrated in Fig. (6.b), show that battery temperature decreases as the number of parallel cells increases, which also leads to a higher overall mass. While the added mass raises the vehicle's rolling resistance and therefore increases the power demand, this effect is outweighed by the reduction in internal resistance due to cell parallelisation.

However, Test 3 also aims to minimize the energy losses in the driving motor. The results show that the optimizer selected a motor size close to the upper limit of the design variable. Although this increases the overall vehicle mass, the additional motor mass is considered beneficial in this case. This outcome reflects the optimizer's preference for maximizing motor power, since it is explicitly included in the objective function through a penalty term.

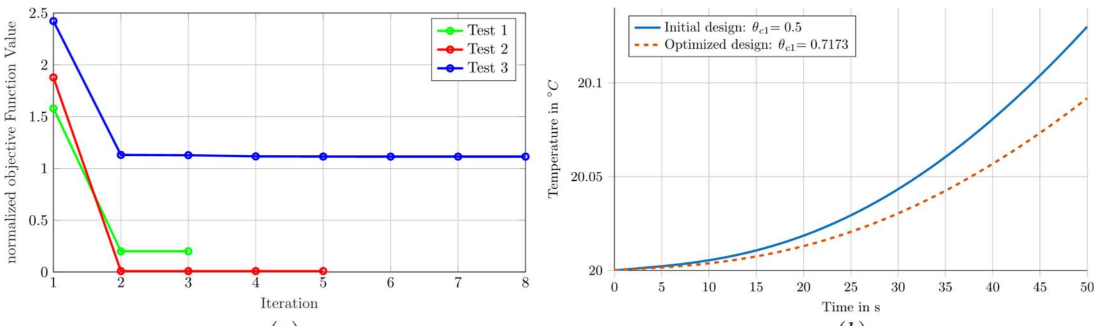

(a) (b)

Figure 6: (a) Convergence plot for the three tests, (b) High-Voltage Battery Temperature (Test 2).

4 Conclusion

This work employs a design methodology for optimization that captures the multi-energy domains of dynamic systems. The approach adopts a graph-based modeling technique to represent the physical behaviour and interactions among components. Within this framework, design alternatives, such as component sizing and topology, are systematically integrated.

The case study investigates an electric bus powertrain under a single operational strategy. The results show that variations in component configurations—specifically changes in motor, pump, and battery sizes, significantly affect the thermal behaviour of the system. As a consequence, the energy demand of the thermal management system may either increase or decrease depending on the design choices.

Future work will extend the framework to incorporate multiple operational strategies, with particular focus on evaluating the impact of powertrain design on thermal management requirements during the regenerative braking phases of the electric bus.

5 References

[1] M. Kumar, I. N. Kar and A. Ray, "State Space Based Modeling and Performance Evaluation of an Air-Conditioning System," *HVAC\&R Research,* vol. 14, no. 5, p. 797–816, 2008.

[2] M. Xu, Z. Zhang, X. Wang, L. Jia and L. Yang, "A pseudo three-dimensional electrochemical--thermal model of a prismatic LiFePO4 battery during discharge process," *Energy,* vol. 80, p. 303–317, 2015.

[3] . H. Lindborg, V. Eide, S. Unger, S. Henriksen and H. A. Jakobsen, "Parallelization and performance optimization of a dynamic PDE fixed bed reactor model for practical applications," *Computers \& chemical engineering,* vol. 28, no. 9, p. 1585–1597, 2004.

[4] J. Garcia, G. Dauphin-Tanguy and C. Rombaut, "Modeling and simulating the dynamic electrothermal behavior of power electronic circuits using bond graphs," *PESC Record. 27th Annual IEEE Power Electronics Specialists Conference,* vol. 2, p. 1641–1647, 1996.

[5] G. Rizzoni, L. Guzzella and B. M. Baumann, "Unified Modeling of Hybrid Electric Vehicle Drivetrains," *IEEE/ASME transactions on mechatronics,* vol. 4, no. 3, p. 246–257, 1999.

[6] J. Allison and D. Herber, "Multidisciplinary Design Optimization of Dynamic Engineering Systems," *AIAA journal,* vol. 52, pp. 691-710, 2014.

[7] J. P. KOELN, "Hierarchical Power Management in Vehicle Systems," in *PhD-Thesis*, Urbana, Illinois, University of Illinois at Urbana-Champaign,, 2016.

[8] C. T., Aksland, A. G. and Alleyne, "Hierarchical model-based predictive controller for a hybrid UAV powertrain," *Control Engineering Practice,* vol. 115, no. 0967-0661, p. 104883, 2021.

[9] D. J. Docimo, Z. Kang, K. A. James and A. G. Alleyne, "A Novel Framework for Simultaneous Topology and Sizing Optimization of Complex, Multi-Domain Systems-of-Systems," *Journal of Mechanical Design,* vol. 142, no. 6, pp. 091701-1- 091701-16, 2021.

[10] C. T. Aksland, T. W. Bixel, L. C. Raymond, . M. A. Rottmayer and A. G. Alleyne, "Graph-Based Electro-Mechanical Modeling of a Hybrid Unmanned Aerial Vehicle for Real-Time Applications," in *2019 American Control Conference (ACC)*, IEEE, 2019, p. 4253–4259.

[11] C. Laird, Z. Kang, K. A. James and A. G. Alleyne, "Framework for integrated plant and control optimization of electro-thermal," *Energy,* vol. 258, no. 124855, pp. 1-14, 2022.

[12] J. Koeln, M. A. Williams, C. Pangborn H. and A. ,. G. Alleyne, "Experimental validation of graph-based modeling for thermal fluid power flow systems," *Dynamic Systems and Control Conference,* vol. 50701, no. V002T21A008, p. 1–10, 2016.

[13] D. J. Docimo and A. G. Alleyne, "Graph-Based Hierarchical Control of Thermal-Fluid Power Flow Systems," in *2017 American Control Conference (ACC)*, Washington, IEEE, 201, p. 2099–2105.

[14] P. J. Tannous and A. G. Alleyne, "Fault Detection and Isolation for Complex Thermal Management Systems," *Journal of Dynamic Systems, Measurement, and Control,* vol. 141, no. 6, p. 061008, 2019.

[15] H. Pangborn, J. P. Koeln, W. A. Matthew et A. G. Alleyne, «Experimental validation of graph-based hierarchical control for thermal management,» *Journal of Dynamic Systems, Measurement, and Control,* vol. 140, n° %110, p. 101016, 2018.

[16] H. Schäfer, T. Hellberg et M. Meywerk, «Simulation-Based Investigation and its Experimental Validation of the Thermal Behaviour of a Battery Electric City Bus,» chez *SAE Technical Paper*, Stuttgard, 2025.